respect to the model parameters $a_1, ...a_K$. The model errors are determined by calculation of contours of constant χ^2 levels around the minimum, and defining confidence limits on the parameters.

A more detailed discussion of model fitting is given in Pearson (1995).

2.5 Overview of the post–correlation processing

In this section, we describe a typical procedure of post–correlation processing of a VLBI dataset. The description will list the main operations performed on the datasets, and software used for this purpose. The complete descriptions of the software used are available in the "AIPS Cookbook" and "Caltech VLBI software guide". AIPS was used for fringe fitting and amplitude calibration. The Caltech VLBI software and DIFMAP were employed for self–calibration and mapping. Normally, obtaining a map implied the following operations:

1. Loading the correlator output from a tape, and converting the data into the form suitable for subsequent fringe fitting. The data were written in FITS[2] format. The data were inspected, and then sorted and indexed, in order to facilitate the computer access to them. The VLBI array geometry model was used for calculation of u, v, w coordinates which are essential for the fringe fitting.

2. Fringe fitting. Global single band fringe fitting was done for Mk II data. Multi band fringe fitting was applied to Mk III data. Residual delay and rate windows were carefully specified, in order to avoid spurious solutions. The reference antenna was selected. The rest of the antennas were assigned individual weights to avoid random re-referencing in the case of the reference antenna failing to provide the required signal–to–noise ratio of the solutions.

3. Preparations for amplitude calibration. The delay and rate solutions were smoothed and applied to the data. Phases were aligned, in preparation for subsequent averaging. The typical averaging time was 60 seconds (the time–step of the data from the correlator was 2 seconds). A file containing calibration information – system temperature logs, gains (or alternatively, antenna temperature logs) – from the participating antennas was prepared.

4. Amplitude calibration. The antenna gains were calibrated and the calibration was applied to the visibilities.

5. Exporting data to the Caltech package. A two–step conversion from the AIPS internal data format to FITS, and then from FITS to "merge"[3] format was done. The visibility weights used by AIPS were converted into the error bars used by Caltech package and DIFMAP.

6. Editing. The data were inspected and bad visibility points were edited out. Overall adjustments of the antenna gains were applied in several cases, using close *uv*–points from different baselines (*uv–crossing*).

---

[2]FITS – *Flexible Image Transfer Standard*

[3]*uv*–data format used by the Caltech VLBI package.

7. Producing an initial model for phase calibration. The source structure was fitted by several Gaussian components, in order to achieve a best guess to be used for calibrating the phases. In some cases, antenna gains were scaled, in order to provide a better convergence of the Gaussian fit.

8. Self–calibration loop. The initial guess was used for phase calibration. Then the "CLEAN" deconvolution was applied, in order to produce a "CLEAN" model of the source. The new model was again used for calibrating the visibility phases. This process continued until a model was produced which provided a satisfactory fit to the *closure phases*, thus locating the emitting areas in the field of view. "CLEAN" windows were placed so that the effects of side lobes would be minimized. Once the source structure was reasonably determined, the antenna gains were also allowed to vary. The gain variation times were gradually made shorter, provided that the noise level and overall quality of the image were improving. If needed, additional editing of the data was performed. When the actual noise in the map was approaching the thermal noise level, or when there was no longer a substantial improvement achieved by means of self–calibration, the final image was produced.

9. Model fitting. For the purpose of subsequent studies of kinematic, flux, and spectral changes in the source, the final dataset was fit by spherical, or Gaussian components; the component fluxes, positions and sizes were extracted from the fit. Uncertainties in the models were estimated through calculations of confidence limits for model parameters.

2.6 VLBI images

In this section, we give an account of the VLBI observations of 3C345, and present maps and Gaussian models for 13 epochs observed at 5, 8, 11, and 22 GHz. A total of 23 radio telescopes located in the Northern hemisphere have participated in the observations. General parameters of the telescopes are summarized in Table 2.1. Tables 2.2–2.3 give a review of all the observations.

2.6.1 Introductory remarks

The morphology and evolution of the parsec–scale jet of 3C345 have been studied extensively from the late seventies. The most complete accounts of the work preceding this dissertation can be found in Biretta, Moore and Cohen (1986), and in Zensus, Cohen and Unwin (1995). The first paper covers the time period from 1979 to 1984. In the second paper, the analysis has been extended until the end of 1988. In both papers, the kinematic and emission properties of the jet are determined by fitting optically thin spherical components to the source structure. Spherical components were chosen for the purpose of facilitating the subsequent calculation of emission properties. Such choice also reflected the common views ascribing the jet components to expanding spherical blobs. In the high dynamic range maps, however, regions of enhanced emission are commonly found to be considerably extended, being rather

Table 2.1: Selected technical parameters of VLBI antennas participated in the observations.

Location / Network		Code[1]	D^2	T^3_{sys5}	T^4_{sys8}	T^5_{sys11}	T^6_{sys22}	R.S.[7]
Effelsberg, Germany	E[8]	B	100m	44	40	55	125	Mk3A
Medicina, Italy	E	L	32m	290	240	395	1090	Mk2,3A
Noto, Italy	E	N	32m	190	1800		1250	Mk2;VLBA
Onsala, Sweden	E	S	25m	992				Mk2,3A
			20m		2071		1586	Mk2,3A
Cambridge, UK	E	E	32m	135			500	Mk2;VLBA
Jodrell Bank, UK	E	J	76m	153				Mk2,3A
			26m	344			1500	Mk2,3A
WSRT[9]	E	W	93m[10]	107	95			Mk2,3A
Metsähovi, Finland	E[11]	V	14m				1423	Mk2;VLBA
Simeiz, Ukraine	E[11]	R	22m	3174			1000	Mk2,3A
Green Bank, USA		G	43m	45	45	45	45	Mk2,3
Haystack, USA		K	36m	55	100	80	70	Mk2,3;VLBA
VLA[12], USA		Y	25m	55	45		500	Mk2,3;VLBA
OVRO[13], USA		O	40m	55	180	70	50	Mk2,3;VLBA
Saint Croix	V[14]	Sc	25m	42	46		186	Mk3;VLBA
Hancock	V	Hn	25m	41	34		96	Mk2,3;VLBA
North Liberty	V	Nl	25m	41	48		105	Mk2,3;VLBA
Fort Davis	V	Fd	25m	42	32		82	Mk2,3;VLBA
Los Alamos	V	La	25m	39	36		95	Mk2,3;VLBA
Pietown	V	Pt	25m	45	37	93	92	Mk2,3;VLBA
Kitt Peak	V	Kp	25m	44	34		104	Mk2,3;VLBA
Owens Valley	V	Ov	25m	36	49		73	Mk2,3;VLBA
Brewster	V	Br	25m	31	40		106	Mk2,3;VLBA
Mauna Kea	V	Mk	25m	38	36		88	Mk3;VLBA

Notes: 1 – abbreviation of the telescope name; 2 – antenna diameter [m]; 3 – receiver system temperature at 5 GHz [Jy]; 4 – receiver system temperature at 8 GHz [Jy]; 5 – receiver system temperature at 11 GHz [Jy]; 6 – receiver system temperature at 22 GHz [Jy]; 7 – recording system; 8 – European VLBI Network; 9 – The Westerbork Radio Synthesis Telescope, The Netherlands; 10 – total collecting area in the phased array mode; 11 – associated member; 12 – The Very Large Array, Socorro, New Mexico; 13 – Owens Valley Radio Observatory, California; 14 – Very Long Baseline Array.

Table 2.2: General parameters of the VLBI observations of 3C345.

Date	ν^1	Mode^2	Correlator	Array Configuration^3	S^4_{tot}	S^5_{peak}
03/31/89	22.3	Mk2	Block-2^6	BLKGYPtO	4.190	1.210
04/06/89	10.6	Mk2	Block-2	BLNKKpPtFdO	7.551	1.375
06/19/91	22.3	Mk2	Block-2	SBLNKGKpPtLaFdNlYO	10.562	7.045
11/11/91	22.3	Mk2	Block-2	BVLNKGKpPtLaFdNlBr	11.496	7.132
06/04/92	5.0	Mk2	Block-2	SBWCJ2LNKGKpPtLaFdNlBrOvYR	6.618	3.076
06/12/92	22.3	Mk2	Block-2	SBRVLGKpPtLaFdNlBrOvY	12.136	5.514
09/16/92	8.4	Mk2	Block-2	SBLNGKpPtLaNlOvBrY	10.586	6.927
11/11/92	22.3	Mk2	Block-2	SVLNGKpPtLaNlBrOvHn	11.161	4.436
02/15/93	22.3	Mk2	Block-2	LVScHnNlPtKpBrY	8.224	3.357
06/16/93	5.0	Mk3	VLBA^7	ScHnNlFdKpPtLaOvBrMk	7.735	5.337
09/11/93	5.0	Mk3	VLBA	SBLNJWKGKpPtLaFdNlYO	6.130	3.630
09/21/93	22.3	Mk3	VLBA	BLJVNKGKpPtLaFdNlYO	6.302	1.981
11/20/93	8.4	Mk3	VLBA	BLSGHnScNlFdKpLaPtBrOvMkY	8.358	4.952

Notes: 1 – observing frequency [GHz]; 2 – recording mode; 3 – participating antennae abbreviated as follows: B – Effelsberg, C – Cambridge, G – Green Bank, J – Jodrell Bank, K – Haystack, L – Medicina, N – Noto, O- OVRO, R – Simeiz, S – Onsala, V – Metsähovi, W – WSRT, Y – VLA, Sc – VLBA (Saint Croix), Hn – VLBA (Hancock), Nl – VLBA (North Liberty), Fd – VLBA (Fort Davis), La – VLBA (Los Alamos), Pt – VLBA (Pie Town), Kp – VLBA (Kitt Peak), Ov – VLBA (Owens Valley), Br – VLBA (Brewster), Mk – VLBA (Mauna Kea); 4 – total "CLEAN" flux [Jy/beam]; 5 – peak flux density [Jy/beam]; 6 – Block-2 correlator, California Institute of Technology; 7 – VLBA Correlator, Socorro.

Table 2.3: Resolution and noise in the VLBI datasets.

Date	ν^1	σ^2_t	σ^3_{obs}	D^4	B^5_{maj}	B^6_{min}	$B^7_{p.a.}$
03/31/89	22.3	0.7	2.8	380:1	0.37	0.17	-16.9
04/06/89	10.6	0.4	4.7	280:1	0.97	0.32	-10.8
06/19/91	22.3	0.5	4.2	1760:1	0.40	0.16	-11.3
11/11/91	22.3	0.5	3.8	1780:1	0.33	0.17	-10.3
06/04/92	5.0	0.1	0.4	7700:1	1.72	0.80	-5.04
06/12/92	22.3	0.5	4.8	1100:1	0.33	0.19	-21.3
09/16/92	8.4	0.2	3.3	2310:1	0.89	0.45	-8.5
11/11/92	22.3	0.6	3.3	1770:1	0.46	0.20	1.2
02/15/93	22.3	1.5	7.4	500:1	0.29	0.22	-15.3
06/16/93	5.0	0.1	0.6	8900:1	1.94	1.35	-8.83
09/11/93	5.0	0.1	0.6	6050:1	1.49	0.84	-11.7
09/21/93	22.3	0.2	2.5	900:1	0.39	0.17	-10.9
11/20/93	8.4	0.1	1.6	2480:1	1.70	0.78	-13.1

Notes: 1 – observing frequency [GHz]; 2 – ideal RMS noise [mJy/beam]; 3 – observed RMS noise [mJy/beam]; 4 – achieved dynamic range of the map; 5 – beam major axis [mas]; 6 – beam minor axis [mas]; 7 – beam major axis position angle (North through East) [deg].

elliptical. While the ellipticity may appear as a side effect of deconvolution, the extension (especially, the one transverse to the jet direction) can signify the idea of plane or oblique shocks existing in the jet. In order for the fits to represent observed structures better, we chose the elliptical Gaussians to be used in model fitting.

With increasing dynamic range of the VLBI maps, the jet appears to be a continuous formation, rather than a collection of bright features. This circumstance may seemingly undermine the value of model fitting. However, given the specifics of VLBI, there is a limited choice of alternatives.

In the case of compact radio sources, VLBI observations are too infrequent and generally not reliable enough to enable pixel–by–pixel analysis of the images. Violent and rapid variability of the sources would require the time gaps between observations to be as short as several weeks, not several months as they are now.

A rough version of the pixel–by–pixel measurements is implemented by Wardle *et al.* (1994). They analyze statistical properties of the "CLEAN" component distribution for the purpose of extracting the positions (mathematically, the centers of gravity) and fluxes of bright features in the jet. The outcome of this method depends on the choice of sky areas for the "CLEAN" components to be counted in, and on possible inclusion of the deconvolution artifacts into the counts. Model fitting avoids dealing with deconvolution problems by operating in the uv–domain, rather than in the image domain. The goodness of fit is determined by the consistency between the observed quantities (amplitudes, closure phases) and their model counterparts. The applicability of model fitting has been tested in a number of works, and this method has been shown to be a successful approach to the detection and measurement of *changes* in the brightness distribution of radio sources (see Conway *et al.* 1994) — an aspect which is the most important in studies of evolution of source emission. These considerations have determined the choice of model fitting for the source structure analysis.

2.6.2 Jet component nomenclature

In this dissertation, we adopt the naming convention invented for 3C345 in the early works of the Caltech group. The core (normally, the Eastern–most component, with the flat or inverted spectral index) is labeled with the letter "D". Superluminal components are labeled with the letter "C" and are assigned numbers indicating the order of their appearances and detections — C1, C2, C3, etc. Identifications of the components have been done on the basis of consistency of their kinematic properties. In some cases, apparently due to sparcity of the VLBI observations and improving angular resolution, intermediate features were detected between two previously established components. Those were usually assigned an index "a". In the data we use, there is one intermediate feature, namely "C3a". Its nature and origins will be discussed in Chapters 3 and 5.

2.6.3 Observations at 22 GHz

Seven of 13 observations have been made at 22 GHz. At this frequency, antenna sensitivities to the atmospheric conditions are very high. To account for changes of the atmospheric opacity during the observations, exceptionally good calibration information is essential. System temperature measurements were done with 15 minutes intervals (one per observing scan), at most of the telescopes. In some cases, significant changes of the atmospheric opacity occured within even shorter time intervals, resulting in increasing noise in the data. For several datasets the opacity effects were corrected, using the algorithm developed by K. Leppänen (1993).

The RMS noise in the maps at 22 GHz does not exceed 7 mJy, and depends on the quality of the data and calibration. The achieved noise level is about 10 times higher than the theoretical expectations from ideal data (see Table 2.3). This is evidence that calibration and deconvolution errors are dominating the 22 GHz maps. The dynamic ranges, measured as the ratio of the peak flux density to the RMS noise, vary from 280:1 to 1780:1. The resolution achieved in the maps is about 0.1 mas. In 3C345 ($z = 0.594$, Hewitt and Burbidge, 1993), this translates into $\approx$0.5 pc.

The individual observations, maps, and model fits are presented below.

March 31, 1989 (1989.24)

The map (Figure 2.8 on page 27) shows the compact core, D, and a jet traced up to 2 mas West from the core. The relatively weak ($S_D = 1.5$ Jy) core is identified by its compactness and positive spectral index $\alpha_{[11-22GHz]} = 0.2$. The jet is not straight, which is clearly seen from the variations of position angles for different components (Table 2.4 on page 28). These twists in the jet have been also observed at the earlier epochs (Zensus *et al.* 1995a) and at higher frequencies (Krichbaum *et al.* 1991). Components C4, C5, and C6 are well defined. The presence of C7 can be guessed from a slight extension of the core. Introduction of this component was required for achieving a satisfactory fit to the observed closure phases.

The low core flux indicates that the source is in a quiescent phase. The 22 GHz flux of 3C345 was declining since 1984, and this decline was detected in both VLBI and single dish observations. The epoch of 1989 is very close to the epoch of minimum total flux at 22 GHz (Terasranta, personal communications).

The RMS noise in the map is 3 mJy, and the peak flux density is 1.2 Jy, resulting in the dynamic range of about 380:1.

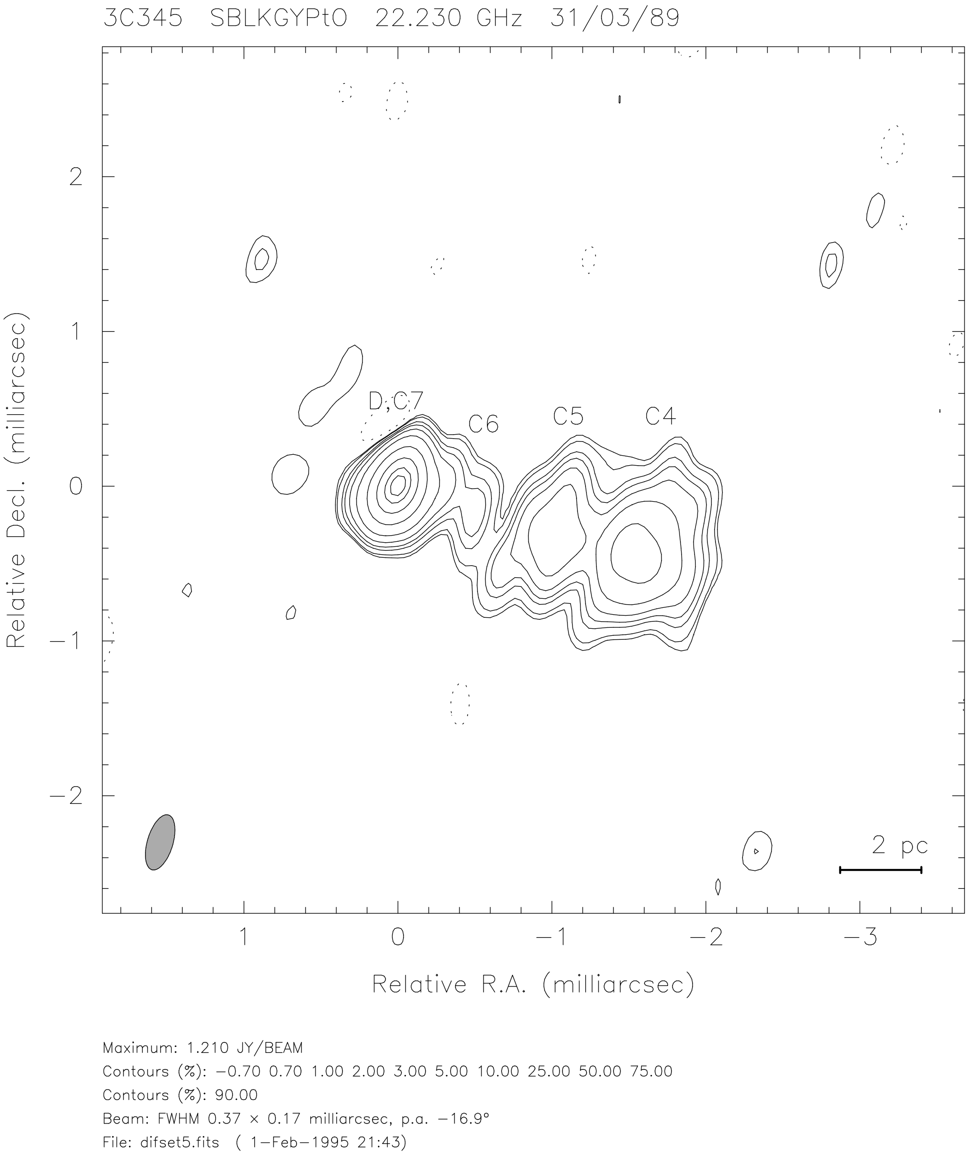

Figure 2.8: VLBI map of 3C345 observed at 22.3 GHz on March 31, 1989.

Table 2.4: Model for epoch 1989.24 at 22.2 GHz.

Name	S [Jy]	δ_S [Jy]	r [mas]	δ_r [mas]	θ [°]	δ_θ [°]	b_{maj} [mas]	$\delta_{b_{maj}}$ [mas]	ϵ	δ_ϵ	ϕ [°]	δ_ϕ [°]	Fit
D	1.488	0.128	0.000	0.000	0.000	0.000	0.121	0.010	0.993	0.118	104.350	0.000	G
C7	0.193	0.023	0.046	0.025	-83.899	7.561	0.064	0.000	0.999	0.084	-113.217	0.000	G
C6	0.282	0.045	0.576	0.134	-97.660	4.645	0.185	0.026	0.994	0.094	34.016	0.000	G
C5	1.050	0.121	1.202	0.014	-109.874	0.821	0.425	0.019	0.990	0.144	89.993	0.000	G
C4	1.295	0.072	1.782	0.008	-102.539	0.306	0.392	0.020	0.989	0.103	-0.012	0.000	G

Total flux $S_{tot} = 4.309 \pm 0.197$

Symbols: S – component flux density; r – component relative distance from the core "D"; θ – component position angle (North through West); b_{maj} – component major axis; ϵ – component axial ratio; ϕ – component major axis position angle (North through West); Fit – type of the fit (G – elliptical Gaussian; S – optically thin sphere). The δ–s indicate the estimated errors for the corresponding parameters. Zero errors indicate that no error estimates were made for the corresponding parameters.

June 19, 1991 (1991.46)

The "CLEAN" map is shown in Figure 2.9 on page 30. The source had gone through a significant evolution, and is seen in the middle of a new outburst giving rise to C7. In the model (Table 2.5 on page 31), the core flux contributes 80% of the total VLBI flux. C7 is still very close to the core, but is already 4 times brighter than it was in 1989. The estimated sizes of the core and C7 are comparable to the distance between them, and this can indicate that the high flux of the core is related to the flux increase of C7. At both epochs, the distances produced by the model fitting for C7 are smaller than the actual resolution in the maps. This fact may be an indication that C7 remained stationary during this time period, and probably was a part of the core complex (for instance, C7 may be located in a vortex of an accretion torus, a possible site of the initial plasma acceleration). Taken at face value, the position measurements yield the upper limit $\beta_{max} \approx 0.4c$ for the motion of C7, while from the resolution considerations, no motions slower than $0.8c$ are reliably detectable at the given time separation between observations.

C6 and C5 are still well detected, albeit their fluxes are low. C4 is detected only marginally, and its flux is distributed over a large area of almost 2 mas in diameter. The size of C5 has also increased substantially, since 1989.

The RMS noise is about 5 mJy, higher than in the previous map. This can be explained by the deconvolution problems in the case of a strong source. Despite the higher RMS noise, the dynamic range of the map exceeds 1700:1 because of the high peak flux density (7.05 Jy) observed in the core.

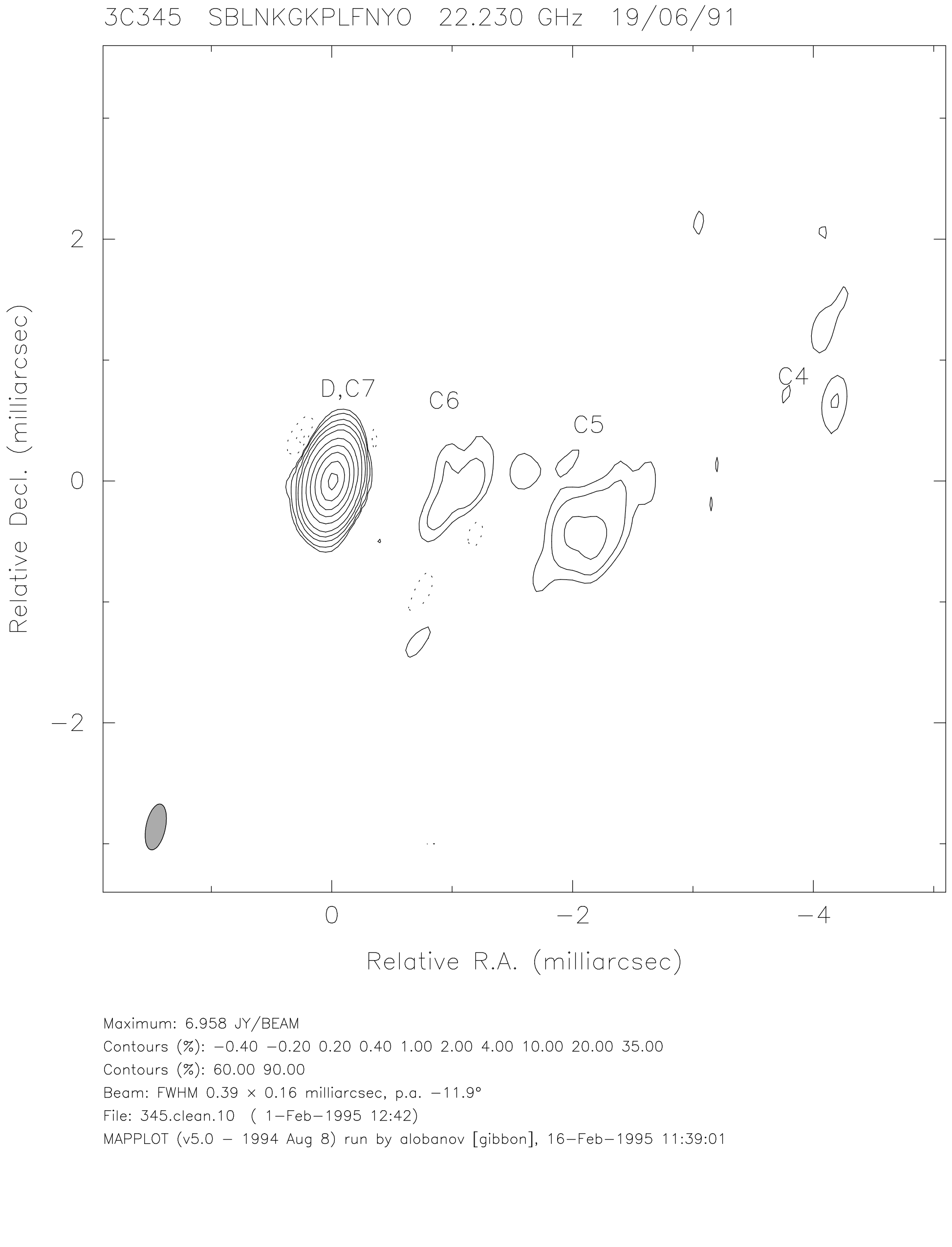

Figure 2.9: VLBI map of 3C345 observed at 22.3 GHz on June 19, 1991.

Table 2.5: Model for epoch 1991.46 at 22.2 GHz.

Name	S [Jy]	δ_S [Jy]	r [mas]	δ_r [mas]	θ [°]	δ_θ [°]	b_{maj} [mas]	$\delta_{b_{maj}}$ [mas]	ϵ	δ_ϵ	ϕ [°]	δ_ϕ [°]	Fit
D	9.596	0.068	0.000	0.000	0.000	0.000	0.143	0.010	1.000	0.000	0.000	0.000	G
C7	0.800	0.043	0.086	0.047	-94.639	7.470	0.130	0.065	1.000	0.000	0.000	0.000	G
C6	0.123	0.036	0.873	0.017	-99.445	9.628	0.180	0.068	1.000	0.000	0.000	0.000	G
C5	0.606	0.140	2.181	0.182	-100.660	2.683	0.750	0.101	1.000	0.000	0.000	0.000	G
C4	0.803	0.000	4.237	0.163	-75.488	2.819	1.845	0.230	1.000	0.000	0.000	0.000	G

Total flux: $S_{tot} = 11.928 \pm 0.165$

Notes: S – component flux density; r – component relative distance from the core "D"; θ – component position angle (North through West); b_{maj} – component major axis; ϵ – component axial ratio; ϕ – component major axis position angle (North through West); Fit – type of the fit (G – elliptical Gaussian; S – optically thin sphere). The δ–s indicate the estimated errors for the corresponding parameters.

November 11, 1991 (1991.86)

In the map (Figure 2.10 on page 33), C7 is still blended with the core, although its presence in the model is essential for reproducing the 180° turns of the closure phases. The flux of C7 has risen to 3.2 Jy, while the core flux declined (Table 2.6 on page 34). The measured separation between the core and C7 is 0.12 mas. The face value calculations give the upper limit on the apparent velocity of C7 $\beta_{max} \approx 2c$, which suggests that the observed flux increase was at least partially caused by the Doppler boosting.

C6, C5, and C4 are still visible, although very weak. Overall, the RMS noise in the map is 4 mJy, the peak flux density is 7.13 Jy, and the dynamic range is almost 1800:1.

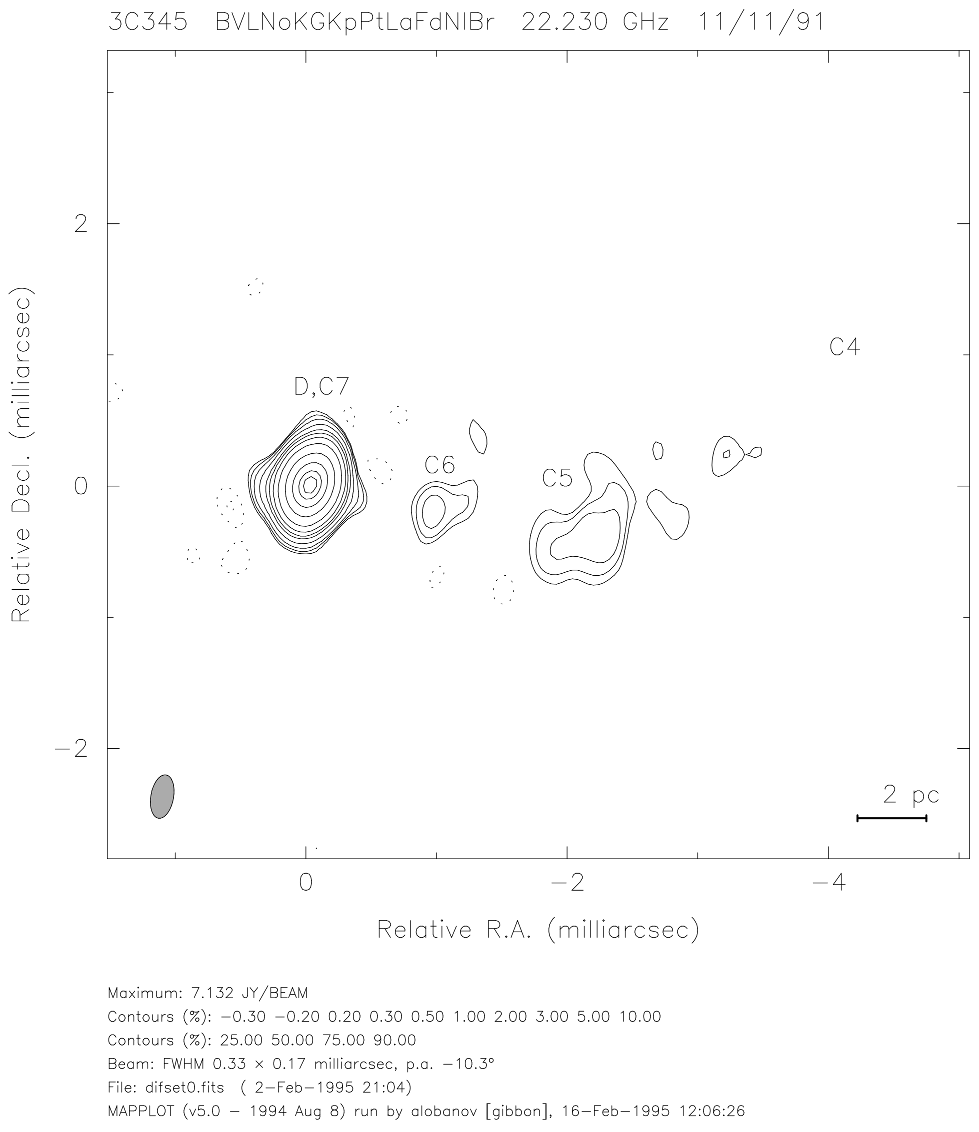

Figure 2.10: VLBI map of 3C345 observed at 22.3 GHz on November 11, 1991.

Table 2.6: Model for epoch 1991.86 at 22.2 GHz.

Name	S	δ_S	r	δ_r	θ	δ_θ	b_{maj}	$\delta_{b_{maj}}$	ϵ	δ_ϵ	ϕ	δ_ϕ	Fit
	[Jy]	[Jy]	[mas]	[mas]	[°]	[°]	[mas]	[mas]			[°]	[°]	
D	7.954	0.496	0.000	0.000	0.000	0.000	0.146	0.005	0.621	0.057	80.568	8.802	G
C7	3.290	0.491	0.125	0.035	-71.046	2.329	0.121	0.007	0.811	0.175	4.666	18.753	G
C6	0.107	0.040	1.024	0.039	-102.268	5.337	0.420	0.140	0.371	0.128	-15.202	69.389	G
C5	0.488	0.076	2.278	0.081	-96.024	1.572	1.097	0.180	0.509	0.173	-54.381	16.265	G
C4	0.266	0.154	4.737	0.465	-76.285	5.320	2.536	0.599	0.403	0.000	147.048	0.000	G

Total flux: $S_{tot} = 12.104 \pm 0.720$

Notes: S – component flux density; r – component relative distance from the core "D"; θ – component position angle (North through West); b_{maj} – component major axis; ϵ – component axial ratio; ϕ – component major axis position angle (North through West); Fit – type of the fit (G – elliptical Gaussian; S – optically thin sphere). The δ–s indicate the estimated errors for the corresponding parameters.

June 12, 1992 (1992.44)

At this epoch, the extension of the core is obvious (Figure 2.11 on page 36), and C7 is detected at almost 0.2 mas separation from the core (Table 2.7 on page 37). At this epoch, the superluminal nature of C7 can already be established. The upper limit on its apparent velocity is unchanged, $\beta_{max} \approx 2c$. The flux of C7 exceeds the flux of the core.

C6 and C5 are still seen in the map. C4 is required by the model fitting for consistency of the model with the amplitude changes on the shortest baselines which are the most sensitive to extended emission. Calculations of the relative brightness of C4 and C5 show that the brightness of C4 is about 2 times lower. Therefore, C4 would be only visible in the map with the contours of 8 mJy/beam or lower. The latter translates into 0.15% contour in the map.

The RMS noise in the map is about 5 mJy and the peak flux density is 5.51 Jy, which translates into the dynamic range of 1100:1.

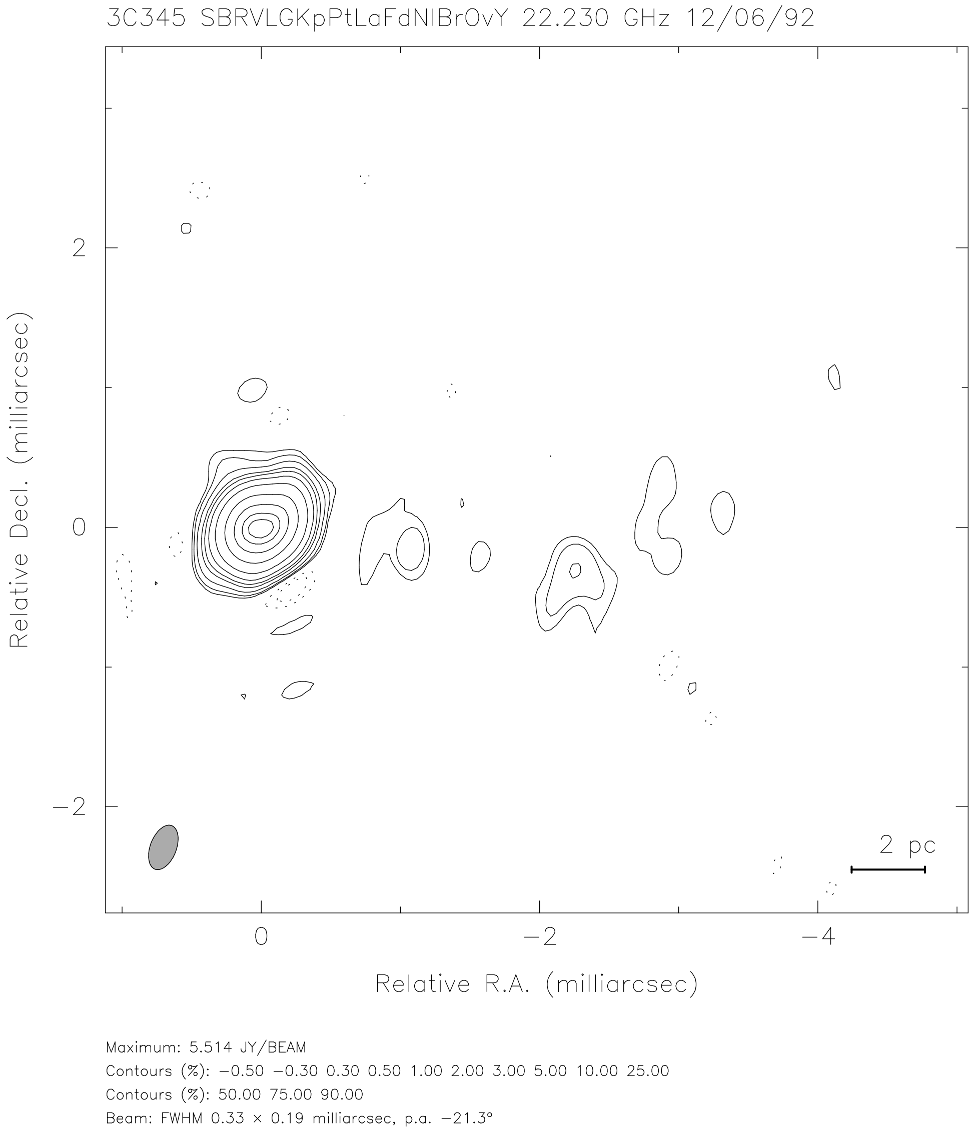

Figure 2.11: VLBI map of 3C345 observed at 22.3 GHz on June 12, 1992.

Table 2.7: Model for epoch 1992.44 at 22.2 GHz.

Name	S	δ_S	r	δ_r	θ	δ_θ	b_{maj}	$\delta_{b_{maj}}$	ϵ	δ_ϵ	ϕ	δ_ϕ	Fit
	[Jy]	[Jy]	[mas]	[mas]	[°]	[°]	[mas]	[mas]			[°]	[°]	
D	6.065	0.358	0.000	0.000	-1.916	0.000	0.177	0.008	0.613	0.000	58.572	0.000	G
C7	6.197	0.359	0.182	0.001	-88.721	1.174	0.205	0.007	0.724	0.000	128.249	0.000	G
C6	0.110	0.047	1.133	0.023	-98.281	3.795	0.256	0.187	0.434	0.000	-8.355	0.000	G
C5	0.290	0.095	2.478	0.187	-94.527	3.595	1.367	0.647	0.227	0.000	-58.669	0.000	G
C4	0.569	0.197	5.152	1.339	-73.817	7.694	3.073	0.400	0.434	0.000	133.735	0.000	G

Total flux: $S_{tot} = 12.321 \pm 0.554$

Notes: S – component flux density; r – component relative distance from the core "D"; θ – component position angle (North through West); b_{maj} – component major axis; ϵ – component axial ratio; ϕ – component major axis position angle (North through West); Fit – type of the fit (G – elliptical Gaussian; S – optically thin sphere). The δ–s indicate the estimated errors for the corresponding parameters.

November 11, 1992 (1992.86)

The map (Figure 2.12 on page 39) has low noise level, allowing for detection of the extended emission. C4 has become visible at the predicted level of 9 mJy (0.20%). The "spotty" appearance of C4 is due to the deconvolution with the small synthesized beam corresponding to the abundance of long baselines in the *uv*–coverage for this dataset. Nevertheless, C4 sums up to 0.4 Jy distributed over the area of about 3 mas in diameter.

C5 is also shaping up more clearly than in the previous maps, and the component is visibly breaking up into several connected spots. This can be caused by the intrinsic evolution in the component, as well as by the deconvolution effects similar to those resulting in the spotty picture of C4.

Both C7 and the core are weaker than they were at the previous epoch (Table 2.8 on page 40). C7 is still brighter than the core, and its spatial separation from the core increases substantially. The decrease in flux of C7 suggests that the maximum in its spectrum has shifted towards lower frequencies. We can expect to find C7 getting brighter at 5 and 8 GHz, for the observations made at epochs close to November, 1992.

The RMS noise is about 3 mJy, the peak flux density is 4.44 Jy, which gives almost 1800:1 for the dynamic range of the map.

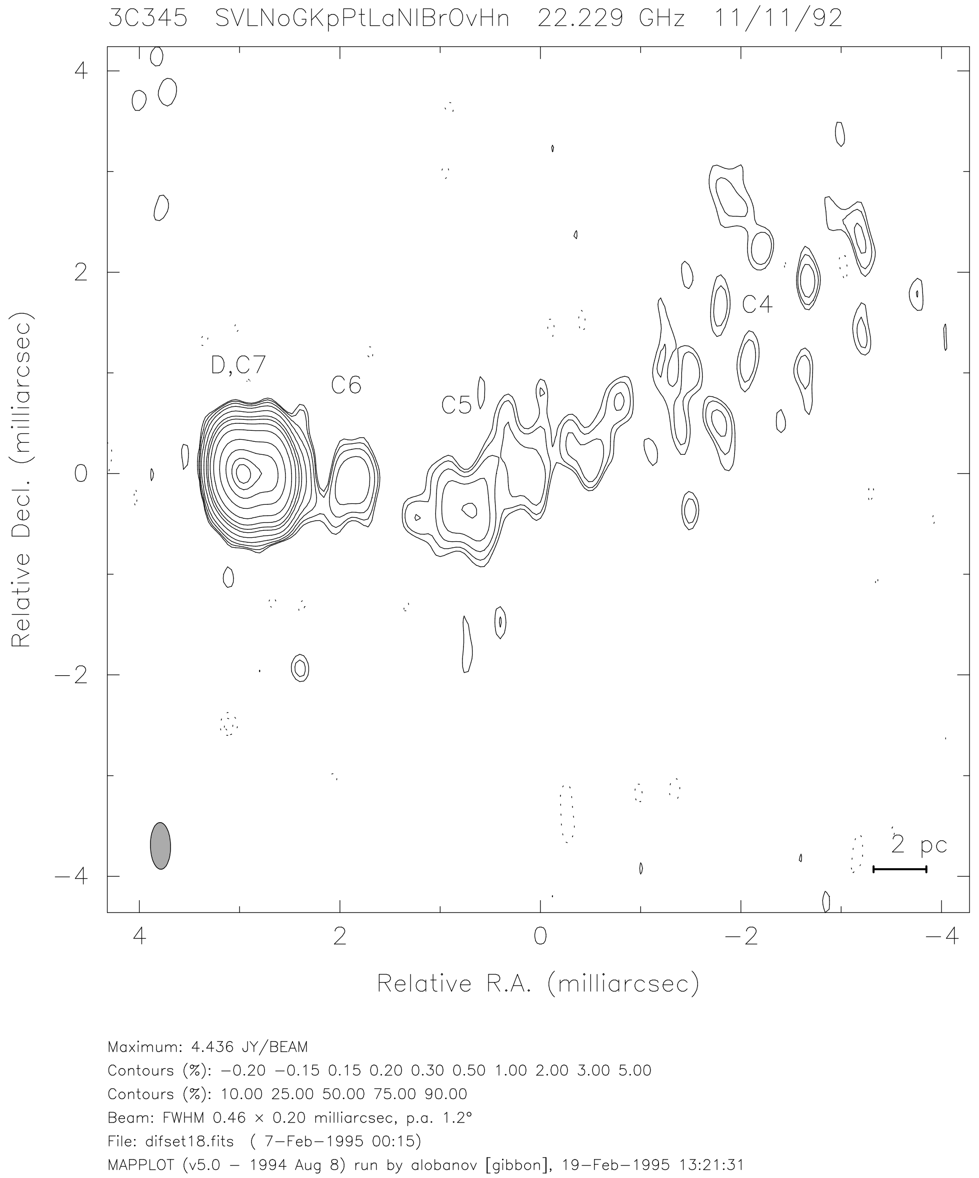

Figure 2.12: VLBI map of 3C345 observed at 22.3 GHz on November 11, 1992.

Table 2.8: Model for epoch 1992.86 at 22.2 GHz.

Name	S	δ_S	r	δ_r	θ	δ_θ	b_{maj}	$\delta_{b_{maj}}$	ϵ	δ_ϵ	ϕ	δ_ϕ	Fit
	[Jy]	[Jy]	[mas]	[mas]	[°]	[°]	[mas]	[mas]			[°]	[°]	
D	5.182	0.293	0.000	0.000	0.000	0.000	0.214	0.007	0.640	0.445	60.932	1.674	G
C7	5.490	0.297	0.278	0.032	-88.412	0.693	0.247	0.009	0.700	0.056	61.336	7.497	G
C6	0.075	0.045	1.033	0.057	-94.026	5.820	0.300	0.100	0.832	0.000	-44.403	0.000	G
C5	0.201	0.090	2.384	0.182	-96.160	3.532	1.170	0.335	0.352	0.179	-60.336	29.845	G
C4	0.412	0.194	4.845	1.114	-75.172	5.064	4.218	0.591	0.387	0.087	-54.597	23.368	G

Total flux: $S_{tot} = 11.369 \pm 0.471$

Notes: S – component flux density; r – component relative distance from the core "D"; θ – component position angle (North through West); b_{maj} – component major axis; ϵ – component axial ratio; ϕ – component major axis position angle (North through West); Fit – type of the fit (G – elliptical Gaussian; S – optically thin sphere). The δ–s indicate the estimated errors for the corresponding parameters.

February 15, 1993 (1993.12)

The map (Figure 2.13 on page 42) shows no traces of extended emission from the old components C4,5,6. This is caused, apparently, by the high noise level of the map and calibration problems. Model fitting yields a two component model (Table 2.9 on page 43) featuring the core D, and C7. A very elongated feature about 2 mas East from the core coincides with one of the prominent side lobes of the dirty beam. Inclusion of this feature into the model fitting did not give any improvement of the fit. Therefore, we leave this feature out.

The decline of both the core and C7 continues. C7 is already considerably weaker than the core. At the same time, its separation from the core is increasing, and the rate of this increase is also growing.

The RMS noise in the map is about 7 mJy. Combined with the peak flux density of 1.98 Jy, it gives about 500:1 for the dynamic range of the map.

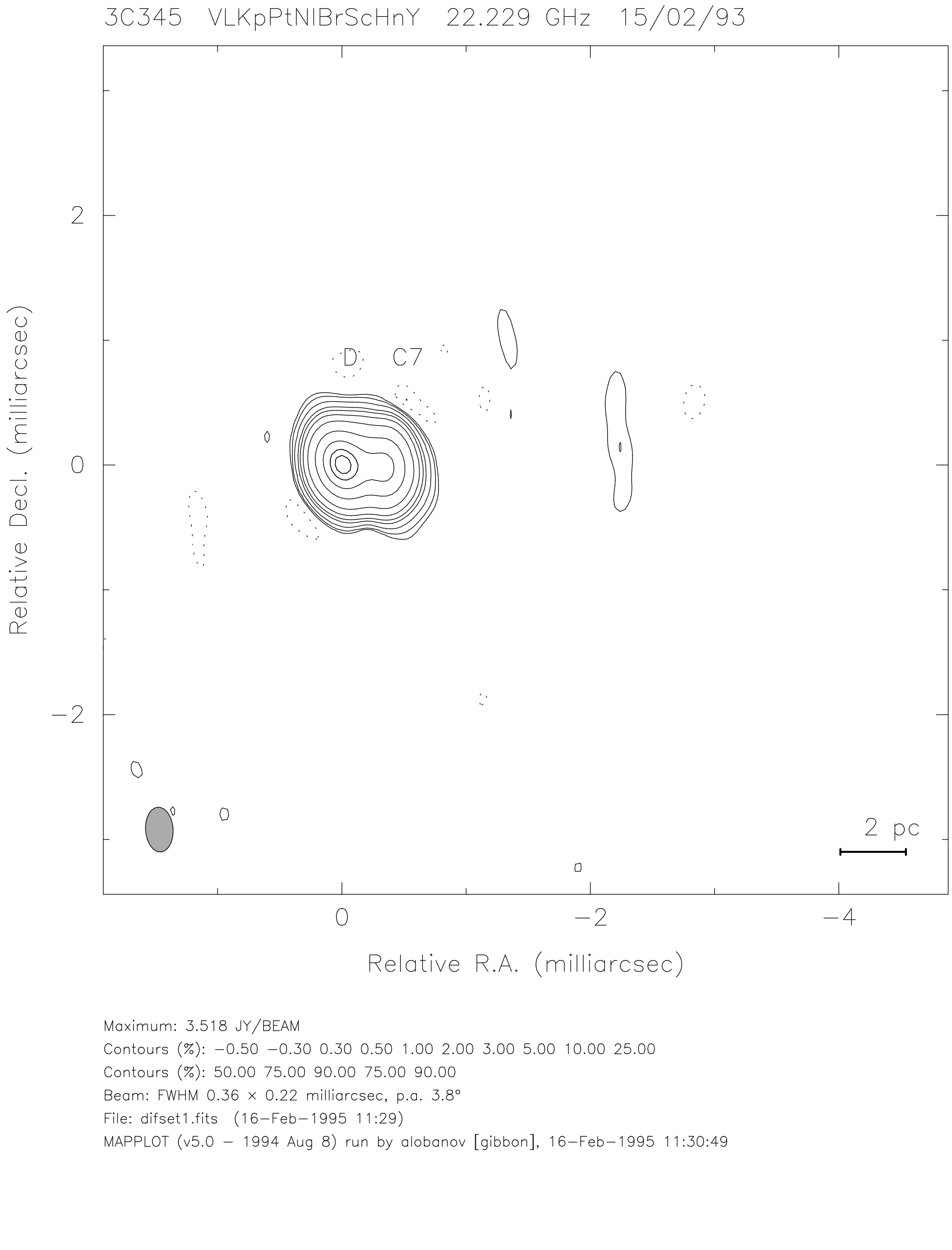

Figure 2.13: VLBI map of 3C345 observed at 22.3 GHz on February 15, 1993.

Table 2.9: Model for epoch 1993.12 at 22.2 GHz.

Name	S [Jy]	δ_S [Jy]	r [mas]	δ_r [mas]	θ [°]	δ_θ [°]	b_{maj} [mas]	$\delta_{b_{maj}}$ [mas]	ϵ	δ_ϵ	ϕ [°]	δ_ϕ [°]	Fit
D	4.753	0.086	0.000	0.000	0.000	0.000	0.205	0.004	0.601	0.033	62.181	2.383	G
C7	3.598	0.099	0.336	0.042	-93.875	0.370	0.234	0.006	0.911	0.038	72.517	12.120	G

Total flux: $S_{tot} = 8.352 \pm 0.132$

Notes: S – component flux density; r – component relative distance from the core "D"; θ – component position angle (North through West); b_{maj} – component major axis; ϵ – component axial ratio; ϕ – component major axis position angle (North through West); Fit – type of the fit (G – elliptical Gaussian; S – optically thin sphere). The δ–s indicate the estimated errors for the corresponding parameters.

September 21, 1993 (1993.72)

The source has become weaker (Figure 2.14 on page 45), and only two components are detectable from the model fitting (Table 2.10 on page 46). C7 is considerably weaker than the core. Its separation has grown to 0.6 mas, resulting in the upper limit for the apparent motion $\beta_{max} \approx 8.7c$. Emission to the west of C7 is too weak to be modeled adequately. We estimate that a reliable detection of this emission would require the sensitivity of about 6 mJy/beam which is just above the 2σ level for the off–source RMS noise level. This can explain the failure of model fitting to allocate Gaussian components into this area.

With the RMS noise of about 2 mJy, and peak flux density 1.98 Jy, the dynamic range of the map is roughly 900:1.

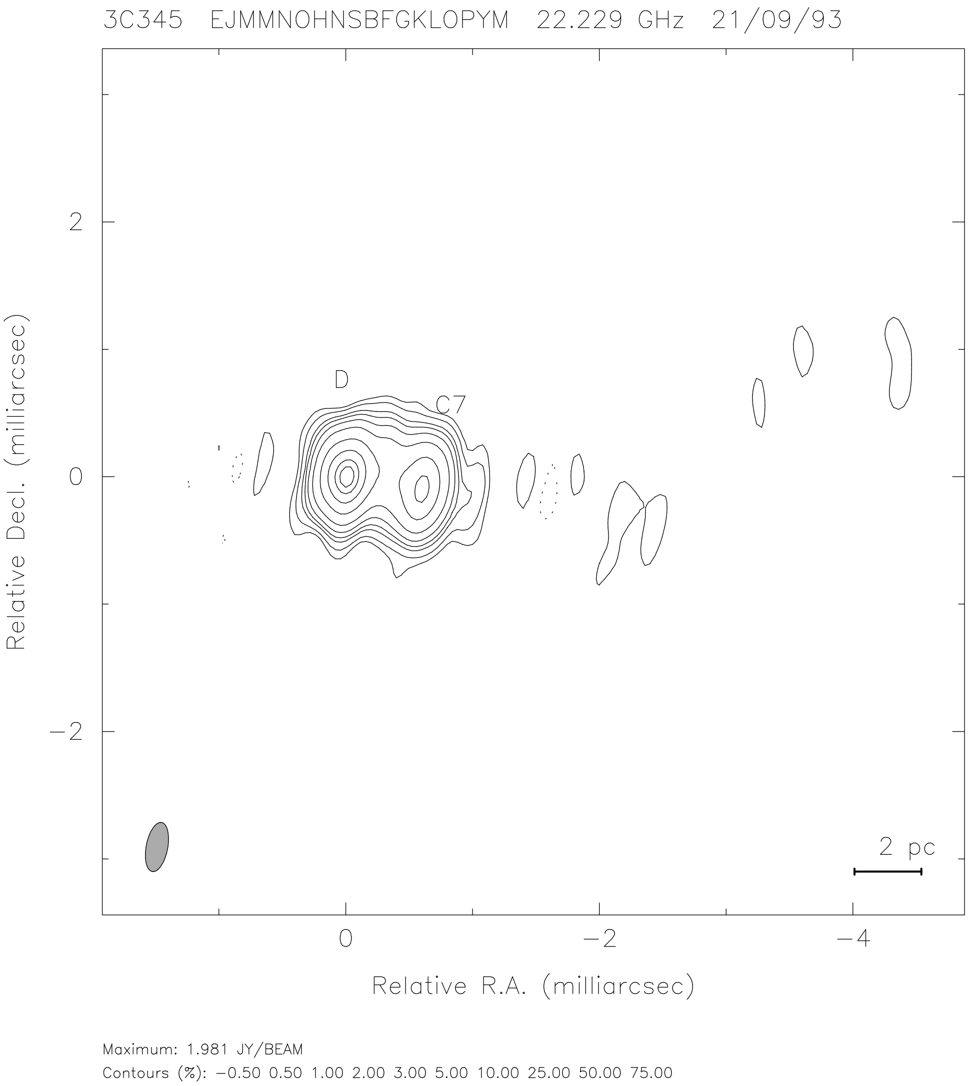

Figure 2.14: VLBI map of 3C345 observed at 22.3 GHz on September 21, 1993.

Table 2.10: Model for epoch 1993.72 at 22.2 GHz.

Name	S [Jy]	δ_S [Jy]	r [mas]	δ_r [mas]	θ [°]	δ_θ [°]	b_{maj} [mas]	$\delta_{b_{maj}}$ [mas]	ϵ	δ_ϵ	ϕ [°]	δ_ϕ [°]	Fit
D	3.914	0.104	0.000	0.000	0.000	0.000	0.236	0.015	0.714	0.061	73.555	4.018	G
C7	2.231	0.117	0.610	0.036	-99.376	1.636	0.243	0.025	0.872	0.094	-25.186	4.786	G

Total flux: $S_{tot} = 6.145 \pm 0.156$

Notes: S – component flux density; r – component relative distance from the core "D"; θ – component position angle (North through West); b_{maj} – component major axis; ϵ – component axial ratio; ϕ – component major axis position angle (North through West); Fit – type of the fit (G – elliptical Gaussian; S – optically thin sphere). The δ–s indicate the estimated errors for the corresponding parameters.

Summary of 22 GHz data

The seven observations of 3C345 at 22 GHz discussed above have covered an important stage of the source evolution — an outburst and emergence of a new superluminal component. There is a possibility that the new component, C7 was detected before its apparent speed became superluminal. However, uncertainties of the modeling do not enable drawing a firm conclusion on this issue. If there is indeed a subluminal stage of the evolution of a jet component, then it may correspond to the location of the jet origin probably coinciding with a vortex of an accretion torus.

The evolution of the older jet components, C6, C5, and C4 was also detected. The general trend of size increase becomes particularly evident in the emission of C4, which causes its brightness to fade away very rapidly. In the two latest epochs, the brightnesses of extended older components have became insufficient for reliable detections.

Figure 2.15 shows all maps at 22 GHz. The separation between individual maps in Figure 2.15 is proportional to the time separatrion between the observation epochs. A map at epoch 1990.41 (Unwin *et al.* 1994) is included, to fill in the gap between 1989.24 and 1991.46.

2.6.4 Observations at 8 and 11 GHz

We have combined two observations at 8.4 GHz and one observation at 10.6 GHz, as the observing frequencies are close, and the resulting *uv*–coverages and sensitivities to the spatial distribution of emission are similar. Increasing coherence time and weaker sensitivity to weather changes during observations make these maps less dependent on frequent system temperature measurements. However, noise in the maps is still dominated by the calibration and deconvolution errors, as it is seen clearly from Table 2.3 on page 24.

April 6, 1989 (1989.26)

The source flux is not very high and distributed almost evenly across the source extension (see Figure 2.16 on page 50, and Table 2.11 on page 51). This fact caused problems for the mapping, as well as for the model fitting. The identification of the core was made by its compactness and positive spectral index between 11 and 22 GHz (see also the discussion of the 22 GHz observation on March 31 1989).

In the map, the jet appears to be continuous, with peaks corresponding to the locations of the bright components. Still, the component locations and sizes are established firmly by the model fitting. We have experienced some difficulties with modeling the component C3 which has an apparently split shape in the map. Our attempts to model this region with two Gaussian components were not successful and caused a decay of the closure phase fit. The latter is strong evidence for errors in locations of the Gaussian components. The closure phase fit improved when

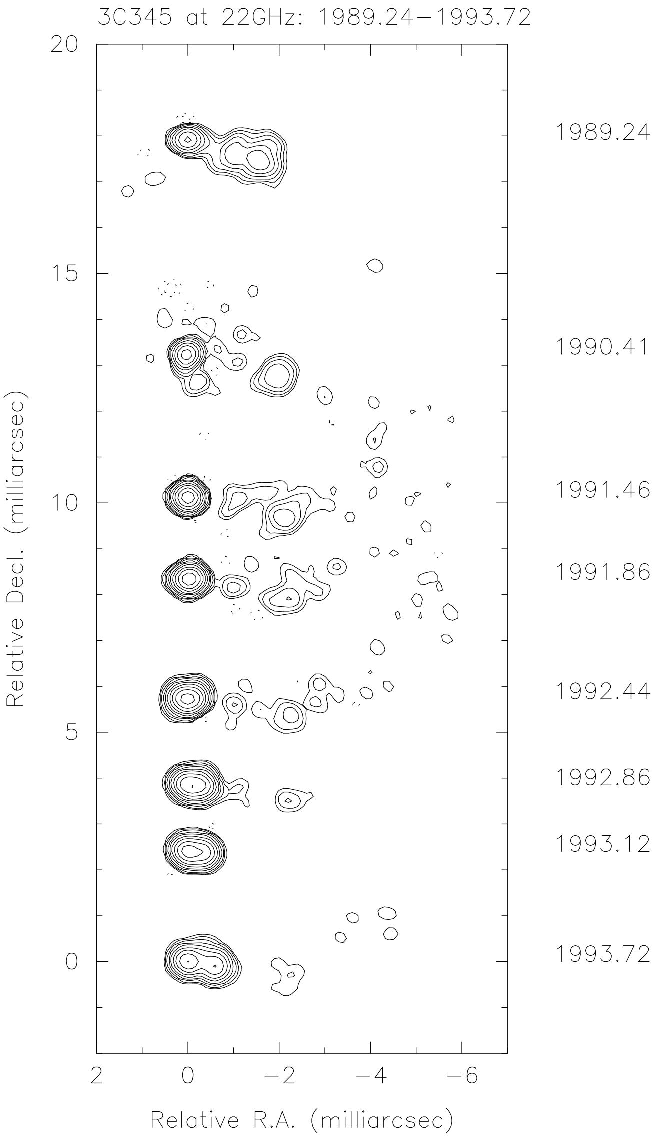

Figure 2.15: Sequence of maps at 22 GHz. Spatial separation between individual maps is proportional to the separation of the observation epochs.

the abovementioned region was modeled by a single Gaussian component of larger extension.

Identifications of C4, C3a, and C3 were made after comparison with maps at 10.6 GHz from previous VLBI observations of 3C345. The origins of C3a and its relation to C4 will be discussed in Chapters 3 and 5.

A substantial twist which the jet experiences at about 4 mas distance from the core appears to be a real and steady feature also detected in maps produced for close epochs from observations at 5 GHz (Unwin & Wehrle 1992).

The RMS noise of the map is about 5 mJy which is higher than the noise in the March 31, 1989 map at 22 GHz. We attribute it to the difficulties with the self–calibration and deconvolution due to the low and evenly distributed flux of the source. Low peak flux density (1.65 Jy), combined with the RMS noise, results in the value of 280:1 for the dynamic range of the map.

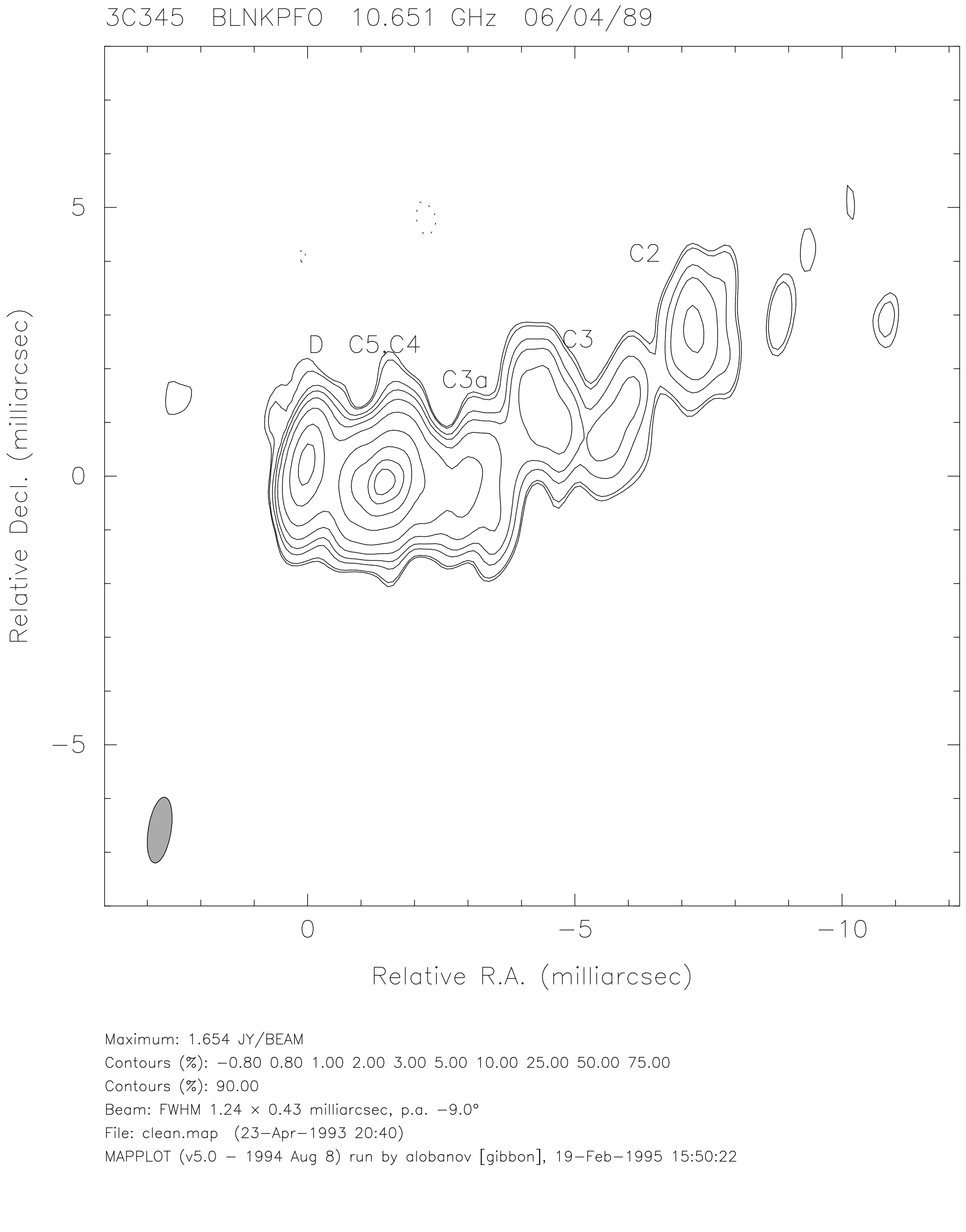

Figure 2.16: VLBI map of 3C345 observed at 10.6 GHz on April 6, 1989.